Post-print version:

Predictive control for mode-switching of reversible solid oxide cells in microgrids based on hydrogen and electricity markets

H. del Pozo Gonzalez, and F.D. Bianchi, and M. Torrell, and L. Bernadet, and J. Eichman, and A. Tarancón, and J.L. Dominguez-Garcia, and O. Gomis-Bellmunt

This work has been published in **International Journal of Hydrogen Energy**:

H. del Pozo Gonzalez, and F.D. Bianchi, and M. Torrell, and L. Bernadet, and J. Eichman, and A. Tarancón, and J.L. Dominguez-Garcia, and O. Gomis-Bellmunt, "Predictive control for mode-switching of reversible solid oxide cells in microgrids based on hydrogen and electricity markets", *International Journal of Hydrogen Energy*, vol. 102, pp. 120-128, 2025.

Final version available at:

URL: https://www.sciencedirect.com/science/article/pii/S0360319924057161

DOI: 10.1016/j.ijhydene.2024.12.497

BibTex:

```
@Article{delPozo2024,
    Title   = {Predictive control for mode-switching of reversible solid oxide
       cells in microgrids based on hydrogen and electricity markets},
    Author  = {Hector del Pozo Gonzalez, and Fernando D. Bianchi, and Marc Torrell,
       and Lucile Bernadet, and Josh Eichman, and Albert Tarancón, and Jose Luis
       Dominguez-Garcia, and Oriol Gomis-Bellmunt},
    Journal = {International Journal of Hydrogen Energy},
    Year    = {2025},
    Number  = {},
    Pages   = {120-128},
    Volume  = {102},
    Doi     = {10.1016/j.ijhydene.2024.12.497}
}
```

Predictive control for mode-switching of reversible solid oxide cells in microgrids based on hydrogen and electricity markets

Hector del Pozo Gonzalez[a,*], Fernando D. Bianchi[b,c], Marc Torrell[a], Lucile Bernadet[a], Josh Eichman[a], Albert Tarancón[a,e], Jose Luis Dominguez-Garcia[a] and Oriol Gomis-Bellmunt[d,e]

[a]Catalonia Institute for Energy Research (IREC), Jardins de les Dones de Negre 1, 2ª, 08930, Sant Adrià de Besòs, Barcelona, Spain
[b]Instituto Tecnológico Buenos Aires (ITBA), Ciudad Autónoma de Buenos Aires, Argentina
[c]Consejo Nacional de Investigaciones Científicas y Técnicas (CONICET), Ciudad Autónoma de Buenos Aires, Argentina
[d]Centre d'Innovacio Tecnologica en Convertidors Estatics i Accionaments (CITCEA), Departament d'Enginyeria Electrica, Universitat Politecnica de Catalunya (UPC), Barcelona, 08028, Spain
[e]Institució Catalana de Recerca i Estudis Avançats (ICREA), Passeig Lluís Companys 23, 08010, Barcelona, Spain

ARTICLE INFO

Keywords:
Reversible solid oxide cells
Model predictive control
Hydrogen microgrids
Transition cycles
Solid oxide electrolysis
Solid oxide fuel cell

ABSTRACT

The use of reversible solid oxide cells (rSOC) as bi-directional Power-to-Gas (P2G) and Gas-to-Power (G2P) devices in microgrids with renewable energy sources has attracted considerable attention in the last years. The present study analyzes the energy management of a rSOC connected in a microgrid, considering hydrogen prices from the European HYDRIX market and electricity prices and demands from the Spanish electrical grid. The energy management strategy, based on model predictive control, determines the optimal path for transitions between SOE and SOFC according to the market. The strategy relies on a model including experimental rSOC transition times, thermal effects, and safety constraints to avoid undesired mode switching. The study was conducted in a scaled grid-connected system including 10 kW solar and wind renewable generation and a rSOC of 4.2-6 kW (SOFC-SOE). The aim is to assess the impact of different renewable energy sources on the performance of rSOC and on the resulting economic balance. The results show that an energy management strategy considering hydrogen markets can reach higher revenue, with increases of ≈4.6% for solar and ≈14.1% for wind, compared to existing algorithms based solely on electricity prices.

1. Introduction

To harness the potential of reversible solid oxide cells (rSOCs) in a green hydrogen-based economy, this technology can store excess energy from renewable sources like solar and wind power in the form of hydrogen. rSOCs have a unique dual-mode operation, functioning both as solid oxide fuel cells (SOFC) and solid oxide electrolyzers (SOE). This versatility is achieved by altering the flow direction and reversing the electrical polarity, allowing rSOCs to switch between generating electrical energy and producing hydrogen, depending on the system's needs [1, 2]. For long-term operation, rSOCs are an ideal technology for small and large-scale applications that require high energy efficiency, durability, and fuel flexibility. When compared to other hydrogen storage technologies like PEM or Alkaline, reversible solid oxide cells offer several distinct advantages, including:

- ☑ *Energy efficiency:* This is attributed to their higher operating temperatures and the direct conversion of chemical energy into electricity.
- ☑ *Fuel flexibility:* They can operate with a wide range of fuels including hydrogen, natural gas, biogas, and liquid fuels.
- ☑ *Tolerance to impurities:* They have the ability to tolerate small amounts of impurities in the fuel, enhancing their versatility.
- ☑ *Thermal stability:* Due to their higher operating temperatures and absence of liquid water inside the stacks, they exhibit greater thermal stability compared to other technologies.

From an industrial prospective, the installation of large-size rSOC systems have already started. On the one hand, a rSOC-based energy storage system formed by 1,920 individual cells have been implemented at Boeing Huntington Beach connected to the Southern California Edison grid [3]. Other example is the Green industrial Hydrogen (GrInHy) project [4], which included an rSOC with a nominal power of ≈ 150 kW in a steel processing plant, with the aim of using the heat excess to reduce costs and increase the overall efficiency, reaching a round-trip value close to 40% [5].

On the academic side, in recent years several works have been published mainly focuses on stack characterization, dynamic behavior, material analysis, degradation efficiencies, etc. However, the operation and control of rSOCs within electric power systems have not widely studied. In different studies with a similar scope, Sorrentino et al. [6, 7] studied the application of rSOCs for supplying a residential complex of 20 houses as load. The different proposed algorithms sought to manage the demand of each of the apartments, establishing the controller's instructions depending on economic and thermal aspects. Huang et al. [8] proposed a model-driven optimal operation strategy for rSOC-based

*Corresponding author:
hdelpozo@irec.cat (H. del Pozo Gonzalez)
ORCID(s): 0000-0002-4270-1353 (H. del Pozo Gonzalez); 0000-0001-7332-6501 (F.D. Bianchi); 0000-0002-3946-1352 (M. Torrell); 0000-0001-6637-0790 (L. Bernadet); 0000-0002-3460-2857 (J. Eichman); 0000-0002-1933-2406 (A. Tarancón); 0000-0002-0483-995X (J.L. Dominguez-Garcia); 0000-0002-9507-8278 (O. Gomis-Bellmunt)

microgrids to minimize costs, considering electricity-heat-hydrogen interactions, mode switching processes, and heat recovery, for its potential application in Denmark's energy islands. Califano et al. [9, 10] proposed control strategies aimed at mitigating the degradation of rSOC working in microgrids, focusing on limiting grid support to achieve more cost-effective performance. Building on this, they developed a multilevel control framework for energy management that optimizes both hydrogen and thermal energy storage, effectively reducing system size and capital costs while minimizing energy waste. Other studies have addressed transitions using simulators with different fidelity levels. For example, Peksen [11] investigated the thermomechanical impacts on rSOCs during the mode-switch, using FEM-based techniques to assess dynamic and static loading effects on materials, providing insights for optimizing rSOC design and reliability.

Expanding the scope to other hydrogen-microgrids not based on rSOC, several studies can be found focused on the behavior of grid-connected hydrogen systems in microgrids, specially employing PEM technology. For instance, the works by Valverde et al. [12, 13], which examines hydrogen-based microgrids with distinct electrolyzer and fuel cell units, often in conjunction with battery storage systems. Also, Abdelghany et al. [14, 15] presented different strategies for efficiently managing a hydrogen-energy storage system in different microgrid configurations powered by solar and wind energy. These studies primarily utilized predictive algorithms to manage the microgrid, aiming to optimize the performance of each system component. Their approach could serve as an inspiration for exploring the potential applications of rSOCs in similar contexts.

Regarding experimental results, several works have focused on characterizing the behavior of the stacks, [16], materials and degradation [17, 18], pressure impacts [19] and transition cycles [20]. This last point is important for designing realistic control strategies, since in long-term operation of grid-connected rSOC, the transition cycles are of great importance. Among the studies that have explored the experimental evaluation of transition cycles, Aicart et al. [20] tested a rSOC system comprising a 1 kW SOE and a 4 kW SOFC during transitions using methane and hydrogen as fuels. Srikanth et al. [21] found that abrupt mode switching between SOFC and SOEC is unviable due to BoP component behavior. Peters et al. [22] showed that rSOC mode transitions from fuel cell to electrolysis can typically occur in under three minutes, though a 10-minute wait is needed for stable steam generator operation. Finally, del Pozo et al. [23] analyzed the different response times of transitions and their impact on microgrid dynamics using a reversible system with a rated 0.7 kW SOFC and 1 kW SOE. The latter will be used for this study.

The key contributions of the article include the following:

1. A novel predictive control strategy for grid-connected rSOC systems that optimizes performance based on variable hydrogen and electricity market prices.
2. Testing the algorithm in both short-term and long-term scenarios within a 10 kW solar and wind-dominated microgrid, demonstrating the benefits of integrating hydrogen market considerations into operational strategies.

The structure of this article is outlined as follows. In Section 2, we delve into the fundamentals of rSOCs, providing an overview of dynamic behavior modeling and presenting a model-experimental comparison of a $0.7 - 1$ kW (SOFC-SOE) reversible solid oxide stack and the grid integration. Moving on to Section 3, we detail the derivation of the predictive controller and elucidate the constraints by the European hydrogen and Spanish electricity markets. The results obtained from applying the predictive controller to real solar and wind energy data profiles are presented in Section 4. Finally, Section 4.2 offers a comprehensive summary of the findings and draws key conclusions from the study.

2. Reversible hydrogen storage with solid oxide cells

2.1. Reversible solid oxide cell dynamics

When the rSOC system operates in fuel cell mode (SOFC), fuel, such as hydrogen or methane, is supplied to the anode, and air is supplied to the cathode. In the case study using hydrogen fuel, hydrogen oxidizes at the anode, releasing electrons to generate electricity according to the reaction:

$$H_2 + O^{2-} \rightarrow H_2O + 2e^-. \tag{1}$$

The resulting oxygen ions migrate through the solid electrolyte, while air flows to the cathode. At the cathode, oxygen ions react with electrons and combine with the fuel, producing water and heat through the reaction

$$\frac{1}{2}O_2 + 2e^- \longrightarrow O^{2-}. \tag{2}$$

In electrolysis mode (SOE), when electricity is supplied to the cells, hydrogen is generated at the anode through the water reduction reaction

$$H_2O + 2e^- \longrightarrow H_2 + O^{2-}, \tag{3}$$

while oxygen is produced at the cathode by the oxidation of water

$$O^{2-} \longrightarrow \frac{1}{2}O_2 + 2e^-. \tag{4}$$

The operation of reversible oxide cells has been dynamically characterized through experiments in our previous works [24, 23]. Table 1 summarizes the most important equations of this model. Briefly, equation (5) describes the voltages of cells operating in SOFC and SOE modes. These voltages are determined by the Nernst equation (6), ohmic losses (8), activation losses (12), and concentration losses (13). The Nernst potential is expressed in terms of the partial

Table 1
Key equations of the lumped model for the 0.7-1 kW SOFC-SOE system [24, 23]

☑ Cells Voltage:

$$\begin{cases} V_{\text{SOFC}} = E_N - \eta_{ohm} - \eta_{act} - \eta_{con}, \\ V_{\text{SOE}} = E_N + \eta_{ohm} + \eta_{act} + \eta_{con} \end{cases} \tag{5}$$

☑ Nernst Potential

$$E_N = E_0 + \frac{R\mathcal{T}}{2F} \cdot \ln\left(\frac{p_{H_2} p_{O_2}^{1/2}}{p_{H_2O}}\right) \tag{6}$$

➲ Reversible Voltage

$$E_0 = 1.2708 + 0.00274\,\mathcal{T} \tag{7}$$

☑ Ohmic Losses

$$\eta_{ohm} = \mathcal{I} \cdot ASR_d \tag{8}$$

➲ Specific Area Resistance

$$ASR = \frac{L_e}{\sigma_{el}} + R_{ct} \tag{9}$$

➲ Electrolyte ionic conductivity

$$\sigma_{el} = \frac{\sigma_{0,el}}{\mathcal{T}} \cdot \exp\left(\frac{-E_{act,el}}{R\mathcal{T}}\right) \tag{10}$$

➲ ASR including degradation terms

$$ASR_d = ASR(1 + \kappa t) \tag{11}$$

☑ Activation losses:

$$\eta_{act} = \underbrace{\frac{R\mathcal{T}}{4\alpha_a F}\sinh^{-1}\left(\frac{i}{2i_{o,a}}\right)}_{Anode} + \underbrace{\frac{R\mathcal{T}}{4\alpha_c F}\sinh^{-1}\left(\frac{i}{2i_{o,c}}\right)}_{Cathode} \tag{12}$$

☑ Concentration losses:

$$\eta_{con} = \underbrace{\frac{R\mathcal{T}}{2F}\ln\left(\frac{p_{H_2O}^{TPB} p_{H_2}}{p_{H_2O} p_{H_2}^{TPB}}\right)}_{Anode} + \underbrace{\frac{R\mathcal{T}}{4F}\ln\left(\frac{p_{O_2}}{p_{O_2}^{TPB}}\right)}_{Cathode} \tag{13}$$

☑ Thermal balance:

$$\Delta\dot{Q} = \dot{Q}_{stack} + \dot{Q}_{ov} - \dot{Q}_{con} - \dot{Q}_{env} \tag{14}$$

$$\text{with} \begin{cases} \dot{Q}_{cell} = \left(\frac{\Delta H}{2F} - V_{cell}\right) i \\ \dot{Q}_{stack} = n_c \left(H_2^{LHV}(2F)^{-1} - V_{cell}\right) i \\ \dot{Q}_{con,j} = \dot{Q}_j^{\mathcal{T}_s} - \dot{Q}_j^{\mathcal{T}_g} \\ \dot{Q}_{env} = k_{l,ov} S_{ov} (\mathcal{T}_s - \mathcal{T}_{amb}) \end{cases} \tag{15}$$

pressures of gases p_x, and the reversible voltage E_0, unlike the initial model, is a function of temperature $\mathcal{T}$ (7). The ohmic losses depend on the current density $\mathcal{I}$ in A/cm^2 and the Area Specific Resistance (ASR), which is influenced by the contact resistance R_{ct} and the electrolyte thickness L_e (9). The electrolyte ionic conductivity σ_{el} (10) is determined by the activation energy of the electrolyte $E_{act,el}$. To account for degradation effects, a linear relation based on the cell degradation rate κ is given in (11). Activation losses (12) are related to the exchange current densities $i_{o,a}$ and $i_{o,c}$ for the anode and cathode, respectively, and are expressed as functions of the temperature and the charge transfer coefficients α_a and α_c at the anode and cathode, respectively. Concentration losses (13) are described by the partial pressures at the Triple-Phase Boundary (TPB) and are modeled using Fick's laws for gases at the anode and cathode. The thermal balance equation (14) establishes ΔQ as the difference between total and stack energies. The symbol $\dot{Q}_{stack}$ represents stack heat which is function of the hydrogen lower heating value H_2^{LHV}, $\dot{Q}_{ov}$ denotes oven heat losses, $\dot{Q}_{con,j}$ corresponds to the j-th gas convection losses, and $\dot{Q}_{env}$ represents environmental losses, which are functions of the oven heat loss coefficient $k_{l,ov}$, and the oven surface S_{ov}. Note that these equations model the electrochemical and thermodynamic processes. A more in-depth explanation and the equations governing the balance of plant and low-level controls, which significantly impact overall system dynamics, can be found in the previous works [24, 23].

Table 2
Table of allowable mode transition in the rSOC.

Current mode \ Next mode	ON	OFF	StB	TCC	SOE	SOFC
ON	-	×	✓	×	×	×
OFF	×	-	✓	×	×	×
StB	✓	✓	-	✓	✓	✓
TCC	×	×	✓	-	✓	✓
SOE	×	×	✓	✓	-	×
SOFC	×	×	✓	✓	×	-

2.2. rSOC mode transitions

The transition among modes in a rSOC may affect the efficiency, safety, and the cell lifespan. Sudden changes in the power delivered and absorbed and also in the operating modes must be avoided. The operating modes in a rSOC and the possible transitions are represented in Figure 1. The red area includes the possible modes in cold conditions and the green area the modes in warm conditions. A rSOC presents six modes: OFF, ON, Stand-by (StB), transition cycle (TCC), SOE and SOFC. Note that in Figure 1, the transition from ON→StB is represented by the heating-up process whereas the transition from StB→OFF is represented by the cooling-down. The arrows in Figure 1 indicates the sequences of possible mode transitions. These possible transitions can be summarized in Table 2, where × denotes a not allowable mode transition and ✓ a allowable mode change. The right plot in Figure 1 presents a comparison between an experimental voltage response and the response obtained with the model in the previous subsection, during a SOFC to SOE transition with composition changes.

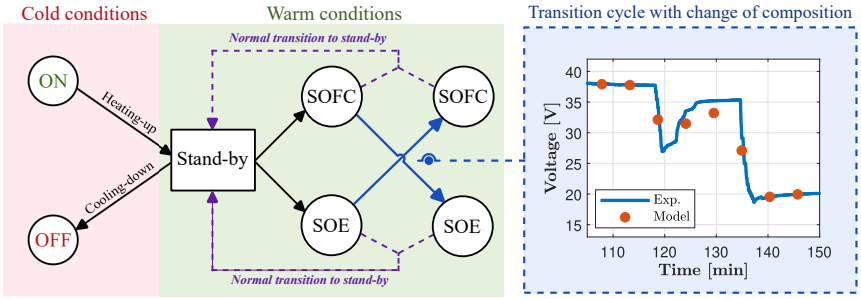

Figure 1: Possible modes and transitions of a rSOC system. The blue area shows a comparison between the experimental response and the model of a SOFC-SOE transition with change of composition of the studied rSOC system.

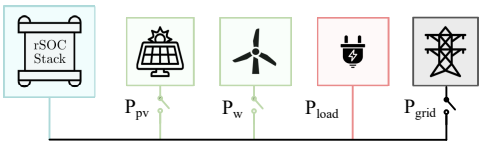

Figure 2: Simplified diagram of the microgrid under consideration with a grid-connected rSOC. Green areas represent units delivering power, while red areas represent units absorbing power.

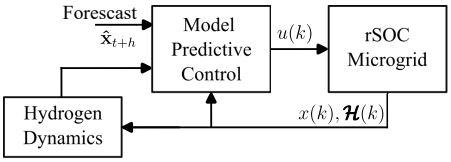

Figure 3: Schematic representation of the system under study and the proposed control strategy.

3. Predictive control for rSOC mode-switching

The main objective of the predictive control strategy is to produce set-points for the rSOC and the grid converter based on the consumption and renewable power generation forecasts, ensuring the local hydrogen tank levels associated with the rSOC system are maintained almost constant. When the rSOC operates in SOE mode, the capacity of hydrogen in the tank increases, whereas when it works in SOFC mode, the capacity decreases as hydrogen is absorbed from the tank. In this study, we assume a continuous water supply for electrolysis mode, hence the water tank dynamics will not be considered. In case hydrogen is also sold to the supply chain, the control strategy can also optimize the total profit by supplying the gas to the tank or to the gas network according to the hydrogen prices.

Figure 2 depicts a simplified diagram of the microgrid under consideration with a grid-connected rSOC, and Figure 3 presents a scheme of the proposed predictive control strategy. The control algorithm receives the forecasts of the wind and solar power generations, the current power consume and the rSOC states, and produces commands for the rSOC and the converter connecting the microgrid with the rest of the grid. At each time step k, the predictive control algorithm solves the following optimization problem:

$$\begin{aligned} &\underset{u(k)}{\text{minimize}} \quad \sum_{j=1}^{4} \lambda_j \mathcal{J}_j(\mathbf{x}(k|N), \mathbf{u}(k|N), \mathbf{d}(k|N)) \\ &\text{subject to} \\ &\mathcal{K}_j(\mathbf{x}(k|N), \mathbf{u}(k|N), \mathbf{d}(k|N)), \quad j = 1, \dots, 7, \end{aligned} \tag{16}$$

where λ_j are weights and N is the prediction horizon. The notation $x(k+i|k)$ denotes the prediction of the variable x at time k and i samples into the future, and $\mathbf{x}(k|N) = [x(k|k)\, x(k+1|k)\, \dots\, x(k+N-1|k)]$. The model states are gathered in the vector x, the control input in u and the rest of inputs in d according to:

$$\begin{aligned} x(k) = \big[\; & \mathcal{H}_{tank}(k) \quad P_{gen}(k) \quad P_{load}(k) \quad \delta_{\mathrm{StB}}(k) \\ & \delta_{\mathrm{SOE}}(k) \quad \delta_{\mathrm{SOFC}}(k) \quad \delta_{\mathrm{ON}}(k) \quad \delta_{\mathrm{OFF}}(k) \\ & \delta_{\mathrm{TCC}}(k) \quad \mathcal{T}(k) \quad V_{cell}(k) \; \big]^T, \\ u(k) = & \big[P_{grid}(k) \quad P_{rSOC}(k) \quad \mathcal{H}_2(k) \quad \psi_{rSOC}(k)\big]^T, \\ d(k) = & \big[\hat{C}_{h2}(k) \quad \hat{C}_{REE}(k)\big]^T. \end{aligned}$$

Every elements of the previous vectors, the terms $\mathcal{J}_j$ in the objective function and the constraints $\mathcal{K}_j$ will be discussed in detail in the next subsections.

3.1. Objective function definition

The objective function in the optimization (16) consists of four terms selected to achieve a trade-off among the power contributions of the grid and the renewable sources considering the energy cost, and a safe operation of the rSOC by limiting the number of transition cycles. Each term is defined as follows:

1. The first term penalizes the power contribution from the grid P_{grid}, since the use of renewable power or energy stored in hydrogen for compensating the consume P_{load} should be prioritized. However, in moments of low renewable power production or low amount of stored hydrogen, the contribution of the network power is necessary to ensure the power balance and the proper microgrid operation. This objective is expressed as

$$\mathcal{J}_1(k) = \sum_{i=0}^{N-1} \left| \hat{C}_{\mathrm{REE}}(k) P_{\mathrm{grid}}(k+i) \right|, \tag{17}$$

with $\hat{C}_{\text{REE}}$ the forecasting of the energy cost in €/kWh. These prices penalize the amount of energy purchased or sold in order to maximize total economic profit. The power exchanged with the grid P_{grid} is positive when the electricity is purchased and negative when it is sold.

2. The second term corresponds to the power balance of the system and to power tracking, since it is desired that the power demanded by the load is always satisfied by the generation P_{gen}, through the tracking error minimization driven by

$$\mathcal{J}_2(k) = \sum_{i=0}^{N-1} \left(P_{load}(k+i) - P_{gen}(k+i)\right)^2. \quad (18)$$

3. The third term is associated with the optimization of the transition cycles of the rSOC. These cycles have a significant impact on the system degradation due to the operation at high temperature. Sudden mode changes should be avoided since the thermodynamic effects inside the cell contributes to the degradation of the rSOC. In addition, optimal operation is desired in both of the operating modes, SOE and SOFC. Therefore, it is necessary to ensure a sufficient dwell time at each mode for the stabilization of internal phenomena without affecting degradation. These objectives are considered in (16) with the term $\mathcal{J}_3$ penalizing the changes between SOE and SOFC modes, and the constraint $\mathcal{K}_1$ to avoid undesired warming-up and cooling-down processes when the stack has reached the warm operation. This is expressed in mathematical terms as:

$$\begin{aligned}\mathcal{J}_3(k) = \sum_{i=0}^{N-1} & \mathcal{W}^P_{\text{SOE}} \left(P_{\text{SOE}}(k+i)\delta_{\text{SOE}}(k+i) - z^*_{\text{SOE}}\right)^2 \\ & + \mathcal{W}^P_{\text{SOFC}} \left(P_{\text{SOFC}}(k+i)\delta_{\text{SOFC}}(k+i) - z^*_{\text{SOFC}}\right)^2 \\ & + \beta^{\text{warming}}_{\text{rSOC}} \sigma^{\text{on}}_{\text{rSOC}}(k+i) + \beta^{\text{cooling}}_{\text{rSOC}} \sigma^{\text{off}}_{\text{rSOC}}(k+i)\end{aligned} \quad (19)$$

where $\mathcal{W}^P_{\text{SOE}}$, $\mathcal{W}^P_{\text{SOFC}}$, $\beta^{\text{warming}}_{\text{rSOC}}$ and $\beta^{\text{cooling}}_{\text{rSOC}}$ are weighting factors. The power absorbed in SOE mode is P_{SOE} and the power produced in SOFC mode is P_{SOFC}, with $P_{\text{rSOC}} = P_{\text{SOFC}}\delta_{\text{SOFC}} + P_{\text{SOE}}\delta_{\text{SOE}}$. The variables δ_{SOFC} and δ_{SOE} takes values 1, if the rSOC works in SOFC or SOE mode, respectively, and 0 otherwise. The constants z^*_{SOE} and z^*_{SOFC} represent the desired power set-points for each mode when activated. The variables $\sigma^{\text{on}}_{\text{rSOC}}$ and $\sigma^{\text{off}}_{\text{rSOC}}$ are given by the constraint:

$$\mathcal{K}_1 : \sigma^{\text{on}}_{\text{rSOC}}(k+i) + \sigma^{\text{off}}_{\text{rSOC}}(k+i) + \sigma^{\text{stb}}_{\text{rSOC}}(k+i) \leq 1 \quad (20)$$

which are related with the possible states shown in the cold area (left red side) of Figure 1, respectively, being σ states of the rSOC at time k to compute the start-warming-up and shut-cooling-down decisions.

4. The last term $\mathcal{J}_4$ in the objective function takes into account the participation of the microgrid in the hydrogen markets. The aim here is to maximize the profit from selling hydrogen. This last term consists of two parts. The first one accounts for the revenue generated by hydrogen sales, and the second one penalizes the deviations from the desired hydrogen tank level. The latter prevents the algorithm from continuously prioritizing the hydrogen sale, which could lead to an excessive deviation of the tank level from the desired value. Mathematically, the objective is expressed as

$$\begin{aligned}\mathcal{J}_4(k) = - \sum_{i=1}^{N-1} & \left|\tau_s \hat{\mathcal{C}}^{\mathcal{H}}_{\text{sell}}(k+i)\dot{m}_{\text{SOE}}(k+i)\right| + \\ & \sum_{i=1}^{N-1} \left(\mathcal{L}_{\mathcal{H}}(k+i) - \mathcal{L}^*_{\mathcal{H}}(k+i)\right)^2,\end{aligned} \quad (21)$$

where τ_s is the sampling time, $\hat{\mathcal{C}}^{\mathcal{H}}_{\text{sell}}$ is the hydrogen sale price forecasted from the HYDRIX market, which account for overall hydrogen process-related expenses such as distribution. The symbol $\dot{m}_{\text{SOE}}$ is the mass flow rate of hydrogen that dependents on the power in SOE mode; and $\mathcal{L}_{\mathcal{H}}$ and $\mathcal{L}^*_{\mathcal{H}}$ denote the measured and desired levels of the hydrogen tank, respectively. Note that the term associated to the hydrogen sale is negative because the optimization problem (16) is stated as a minimization. To consider cases in which the system does not participate in the hydrogen market, the price $\hat{\mathcal{C}}^{\mathcal{H}}_{\text{sell}}$ is set to zero.

3.2. Constraints definition

The rest of constraints $\mathcal{K}_j$ in (16) are stated as follows, where in all expressions $\ell = k, \ldots, k+N-1$:

1. First, the rSOC dynamics is governed by

$$\mathcal{K}_2 : \begin{cases} \mathcal{H}_{tank}(\ell+1) = \mathcal{H}_{tank}(\ell) - \tau_s \left(\delta_{\text{SOFC}}(\ell)\dot{m}_{\text{SOFC}} - \delta_{\text{SOE}}\dot{m}_{\text{SOE}}\right)\left(1 - \delta_{gg}(\ell)\right) \\ \mathcal{H}_{gg}(\ell) = \tau_s \delta_{gg}\delta_{\text{SOE}}(\ell)\dot{m}_{\text{SOE}}(\ell) \end{cases} \quad (22)$$

where $\mathcal{H}_{tank}$ is the amount hydrogen stored in the tank in kilograms for a proper operation of the rSOC, $\mathcal{H}_{\text{gg}}$ the amount sold to the gas grid, $\dot{m}_{\text{SOFC}}$ and $\dot{m}_{\text{SOE}}$, the mass flows in SOFC and SOE modes, respectively. The variable δ_{gg} takes value 1 in case hydrogen is sold and 0 otherwise. In addition, the hydrogen amounts should satisfy

$$\mathcal{K}_3 : \mathcal{H}^{\min}_{tank} \leq \mathcal{H}_{tank}(\ell) \leq \mathcal{H}^{\max}_{tank}, \quad (23)$$

$$\mathcal{K}_4 : \mathcal{H}^{\min}_{gg} \leq \mathcal{H}_{gg}(\ell) \leq \mathcal{H}^{\max}_{gg}. \quad (24)$$

2. Next, in pursuit of producing and utilizing green hydrogen from renewable sources instead of relying on energy from the grid, we impose a limitation on the power demanded to the grid (energy purchased) and the power injected (energy sold) should satisfy:

$$\mathcal{K}_5 : -0.6\, P^n_{gen} \leq P_{grid}(\ell) \leq P^{\max}_{grid}, \quad (25)$$

where P^n_{gen} is the total rated renewable power (photovoltaic or wind) and $P^{\max}_{\text{grid}}$ the upper limit of the power converter connecting the microgrid to the grid. Notice that P_{grid} is negative when power is sent to the grid and positive otherwise. The limitations of the power converter also affect the maximum amount of hydrogen that can be injected into the supply chain, as the maximum hydrogen generation, $\mathcal{H}_{\text{gg}}$, is limited by

$$\mathcal{K}_6 : \mathcal{H}_{\text{gg}}(\ell) \leq \left(P_{\text{gen}} + P^{\max}_{\text{grid}}\right)\eta_{\text{SOE}}(\ell), \tag{26}$$

where η_{SOE} is the efficiency in SOE mode.

3. Changes of operating modes must be limited and the control algorithm must consider the transition constraints discussed in Section 2.2. To include these constraints in the optimization problem (16), let us define the variables:

$$\delta_j(\ell) \in \{0, 1\}$$

where $j \in \{\text{ON}, \text{OFF}, \text{StB}, \text{TCC}, \text{SOE}, \text{SOFC}\}$, the six modes described in Section 2.2. These variables take value 1 if the rSOC works in the j mode and 0 otherwise.

We split the mode constraints into cold and warm conditions (red and green areas in Figure 1, respectively). Thus, the constraint on the possible operating modes in cold conditions can be stated as

$$\mathcal{K}_7 : \begin{cases} \delta_{\text{ON}}(\ell) + \delta_{\text{StB}}(\ell+1) \leq 1, \\ \delta_{\text{OFF}}(\ell) + \delta_{\text{StB}}(\ell+1) \leq 1, \\ \delta_{\text{ON}}(\ell) + \delta_{\text{OFF}}(\ell) + \delta_{\text{StB}}(\ell) = 1, \end{cases} \tag{27}$$

On the other hand, the transitions constraint in warm conditions can be stated as

$$\mathcal{K}_8 : \begin{cases} 1 = \delta_{\text{StB}}(\ell) + \delta_{\text{TCC}}(\ell) + \\ \qquad \delta_{\text{SOE}}(\ell) + \delta_{\text{SOFC}}(\ell). \end{cases} \tag{28}$$

This ensures that only one operating mode is active at any instant ℓ, and the reactor is kept in warm conditions. To avoid infeasible transitions, as depicted by the red crosses in Table 2, we define the constraints:

$$\mathcal{K}_9 : \begin{cases} \delta_{\text{SOE}}(\ell) + \delta_{\text{SOFC}}(\ell+1) \leq 1, \\ \delta_{\text{SOFC}}(\ell) + \delta_{\text{SOE}}(\ell+1) \leq 1, \\ \delta_{\text{SOE}}(\ell) + \delta_{\text{TCC}}(\ell+1) \leq 1, \\ \delta_{\text{SOFC}}(\ell) + \delta_{\text{TCC}}(\ell+1) \leq 1, \end{cases} \tag{29}$$

In order to ensure that the operation in TCC mode is followed by the operation in SOE or SOFC mode, we define the constraints:

$$\mathcal{K}_{10} : \begin{cases} \delta_{\text{TCC}}(\ell) - \delta_{\text{SOE}}(\ell+1) \leq 0, \\ \delta_{\text{TCC}}(\ell) - \delta_{\text{SOFC}}(\ell+1) \leq 0, \end{cases} \tag{30}$$

To limit the number of transitions between SOE and SOFC modes, let us define the difference matrix operator of dimension $(N-1) \times N$:

$$\boldsymbol{\mathcal{D}} = \begin{bmatrix} 1 & -1 & 0 & \cdots & 0 \\ 0 & 1 & -1 & \cdots & 0 \\ \vdots & \vdots & \ddots & \ddots & \vdots \\ 0 & \cdots & 0 & 1 & -1 \end{bmatrix}. \tag{31}$$

Then, the limit in the number of mode transitions can be imposed as:

$$\mathcal{K}_{11} : \begin{cases} \boldsymbol{\delta}_{\text{SOE}}(k|N)\boldsymbol{\mathcal{D}}^T\boldsymbol{\mathcal{D}}\boldsymbol{\delta}_{\text{SOE}}(k|N)^T \leq \alpha, \\ \boldsymbol{\delta}_{\text{SOFC}}(k|N)\boldsymbol{\mathcal{D}}^T\boldsymbol{\mathcal{D}}\boldsymbol{\delta}_{\text{SOFC}}(k|N)^T \leq \alpha, \end{cases} \tag{32}$$

where α is a positive scalar. This constraint limits the maximum allowable number of transitions under warm conditions as denoted in Table 2. These transition constraints are similarly defined in other works related to rSOC mode-switching where only warm operation is considered, see e.g. [8, 25].

4. All time, the generated power must be sufficient to meet the losses and load requirements to ensure the power balance, therefore:

$$\mathcal{K}_{12} : \begin{cases} 0 = P_{\text{gen}}(\ell) + P_{\text{grid}}(\ell) + P_{\text{SOFC}}(\ell)\delta_{\text{SOFC}}(\ell) \\ \quad - P_{\text{SOE}}(\ell)\delta_{\text{SOE}}(\ell) - P_{\text{load}}(\ell) \\ \quad \underbrace{-P_{\text{StB}}(\ell)\delta_{\text{StB}}(\ell) - P_{\text{TCC}}(\ell)\delta_{\text{TCC}}(\ell)}_{\text{passive stack losses during } P_{\text{rSOC}} = 0}, \end{cases} \tag{33}$$

where P_{TCC} and P_{StB} are the passive power losses during each mode from the balance of plant elements.

The remaining constraints aim to ensure safe operation and minimize degradation of the rSOC.

5. Increments in the stack temperature must not exceed 30°C during a time step τ_s, since sudden temperature changes may cause critical problems such as cell rupture or a hydrogen leak. In these cases, power system operations must cease, stopping current injection or power extraction, and revert to open-circuit voltage (OCV) to ensure safety. This constraint is imposed as

$$\mathcal{K}_{13} : \mathcal{T}(\ell) - \mathcal{T}(\ell-1) \leq 30°\text{C}, \tag{34}$$

where $\mathcal{T}$ is the stack temperature.

6. In order to minimize losses due to stack degradation, the voltage must be kept between $0.6\,V_{cell}$ (SOFC) and $1.4\,V_{cell}$ (SOE), that is,

$$\mathcal{K}_{14} : 0.6\,V_{cell} \leq V_{cell}(k+i) \leq 1.4 V_{cell}, \tag{35}$$

where V_{cell} is the volt per cell.

3.3. Forecasting of hydrogen and electricity prices and power balance

Most of the existing microgrid studies assume that the stored hydrogen is contained entirely in a single tank. Consequently, the limits of hydrogen generation and storage are determined by the tank capacity. This usually requires adding a battery system to ensure the power balance when the tank is full or empty. Here, we take a different approach by considering the participation of the rSOC microgrid in the hydrogen and electricity markets. That is, the hydrogen production can be stored or sold according to the hydrogen and electricity prices. For this purpose, a forecaster is needed to properly estimate the hydrogen and electricity prices in the prediction horizon. We employ the Holt-Winters' method, which offers a versatile framework for predicting time series data with trends and seasonal patterns. This method is capable of effectively capturing periodic fluctuations and is commonly utilized for short-term forecasts in sales or demand time series data [26]. Here, the forecaster is used to estimate the matrix $\mathbf{d}(k|N)$ including the hydrogen and electricity prices, $\mathcal{C}_{h2}$ and $\mathcal{C}_{REE}$, respectively. The method uses the following expressions to estimate the MPC inputs at each instant $\ell = k, \dots, k+N-1$:

$$y^{(q)}(\ell) = \alpha\left(z^{(q)}(\ell) - s^{(q)}(\ell - m)\right) + (1-\alpha)\left(y^{(q)}(\ell-1) + b^{(q)}(\ell-1)\right), \tag{36}$$

$$b^{(q)}(\ell) = \beta\left(y^{(q)}(\ell) - y^{(q)}(\ell-1)\right) + (1-\beta)b^{(q)}(\ell-1), \tag{37}$$

$$s^{(q)}(\ell) = \gamma\left(z^{(q)}(\ell) - y^{(q)}(\ell)\right) + (1-\gamma)s^{(q)}(\ell-m), \tag{38}$$

$$\hat{z}^{(q)}(\ell+h) = y^{(q)}(\ell) + h\cdot b^{(q)}(\ell) + s^{(q)}(\ell - m + h), \tag{39}$$

where $\hat{z}$ denotes the smoothed value, b the trend component, s the seasonal component, and y the measured value. The symbols α, β, and γ correspond to the smoothing parameters. The variable m represents the number of periods in a seasonal cycle, while h is the seasonal component index used for adjusting the seasonal effect in the forecast. The superscripts (q), with $q = 1, 2$, correspond to the profiles $\mathcal{C}_{h2}$ and $\mathcal{C}_{\text{REE}}$, respectively. That is,

$$d(k|i) = \begin{bmatrix} \hat{z}^{(1)}(k|i) \\ \hat{z}^{(2)}(k|i) \end{bmatrix} = \begin{bmatrix} \hat{\mathcal{C}}_{h2}(k|i) \\ \hat{\mathcal{C}}_{\text{REE}}(k|i) \end{bmatrix}.$$

An example of the forecaster's performance for the European Energy Exchange (EEX) HYDRIX hydrogen market [27] is shown in Figure 4, where the real values depicted in blue and the predicted values in orange.

4. Results

To conduct case studies close to real scenarios, we analyze the control performance using renewable generation data from solar and wind energies in separate microgrids. The profiles are sourced from two distinct weather stations

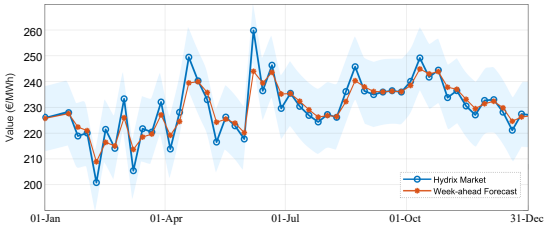

Figure 4: Evolution of annual market price of hydrogen based on HYDRIX [27] in €/MWh. The blue line corresponds the real prices, whereas the orange line to the values predicted by the forecaster. The shaded blue region indicates the confidence intervals.

Table 3
Main parameters of the studied microgrid.

Microgrid parameter	Symbol	Value	Units
Nominal Power Generation	P^n_{gen}	10	kW
SOFC Power	P_{SOFC}	6×0.7	kW
SOE Power	P_{SOE}	6×1	kW
Peak Load	M_s	3.5	kW
H_2 Tank Capacity	$\mathcal{H}^{max}_{tank}$	6.5	kg
H_2 Desired Level	$\mathcal{L}^*_{\mathcal{H}}$	85%	-
Prediction Horizon	H_p	10	-
rSOC Stack Parameter			
Cells Area	A_s	63	cm^2
Stack Mass	M_s	5.5	kg
Number of Cells	n_c	30	-
Oven Power	P_{ov}	2.75	kW
Electrolyte Thickness (8YSZ)	L_e	10	μm
Contact Resistance	R_{ct}	0.3	Ω
Degradation Rate	κ	1.2	$m\Omega cm^2/kh$

in Catalonia, Spain. The wind series were interpolated the from a location near Serra de Montsant, with approximate coordinates of (41°15'05"N, 0°45'56"E), using a Intertek 10 kW small wind turbine sourced from the OpenFAST repository [28]. The solar power generation profiles were obtained from irradiation data from a location near Mataró, with approximate coordinates of (40°46'43"N, 0°30'14"E).

The objective of these scenarios is to show the robustness and adaptability of the proposed control algorithm under different renewable generation profiles.To ease the comparisons, the next figures present the same variables for all the scenarios: the renewable generation, the involved system powers and the dynamics of the generated or absorbed hydrogen. In these figures, it is interesting to observe which renewable energy source requires more power from the grid. This will allow us to determine the overall benefits over time provided by the optimal control of the rSOC depending on the type of power source: wind or solar. The simulations were performed in MATLAB/Simulink, and the controller was implemented using YALMIP [29] and GUROBI [30]. The parameters corresponding to the dynamics of the microgrid, and the control settings are listed in Table 3. A complete set of parameters related to the reversible solid oxide stack model, along with the corresponding equations and their links, can be found in [24, 23].

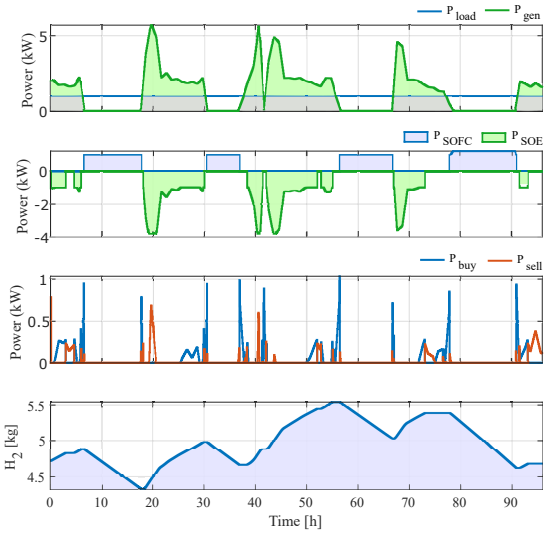

Figure 5: Example demonstrating adherence to transition times between Solid Oxide Electrolyzer (SOE) and Solid Oxide Fuel Cell (SOFC) modes. The simulation is conducted using constant load and low irradiance solar profiles over selected February days, considering only electricity prices.

4.1. Event analysis in wind- and solar-dominated microgrids

To validate the controller's functionality and ensure compliance with transition constraints, some events are aimed to be analyzed with both solar and wind profiles.

The first case study was conducted under constant load and low irradiation days in February in order to assess these aspects on the transition cycles. The upper plot in Figure 5 displays the generation profile with green, the power demand with blue line, and the difference with gray areas. It can be seen that, during periods without solar generation, the fuel cell maintains a constant power contribution. This leads to downward ramps in the tank dynamics, as can be observed in bottom plot, indicating hydrogen consumption for electricity generation. The energy purchased (blue line) and the energy sold (red line) are shown in the second plot from the bottom. The peak energy purchases from the grid coincide with transition periods in order to cover the power demand. On the other hand, the peaks in P_{sell} correspond to the grid contributions to cover the electrolyzer's inability for responding to generation peaks. An analysis of transitions shows that the transition times between modes are met. A detailed examination of rSOC voltage dynamics around the 70-hour mark illustrates correct behavior during direct mode transitions, minimizing standby mode operation. This case study demonstrates a notable increase in energy sold to the grid and greater participation in hydrogen markets. However, fuel cell operation cycles remain prominent due to solar energy's daytime contribution.

Figure 6 presents the results corresponding to a scenario where the renewable power comes from a wind turbine, and the profit is optimized considering only the electricity prices. During the initial hours, with low electricity prices, the SOE mode is activated to fill the hydrogen tank, as its levels are not yet full. As electricity prices rise, the SOFC mode becomes more prominent, as depicted in the third plot from the bottom. Consequently, the amount of energy sold, shown in the second plot from the bottom, increases. This sold energy comprises both the excess renewable power and the electricity generated in SOFC mode. This shift significantly impacts the tank dynamics, as seen in the bottom plot, where hydrogen levels decrease during periods of energy sales to the grid.

In Figure 7, it can be observed the results for a scenario similar to the previous one, but now considering the electricity and the hydrogen markets in the profit optimization. The top plot shows a marked increase in the trend of the hydrogen market price (blue line) at the instant t_1, while electricity prices (red line) remain with a lower revenue. Given the high wind generation levels, which can supply the load, the electrolysis mode is predominant. When the forecast detects a potential increase in hydrogen prices, the system activates the sale to the grid in SOEC mode. From that moment, the hydrogen tank level is maintained at the level reached up to t_1 (highlighted in blue in the bottom plot), while the sale to the grid (highlighted in red) begins with a significant contribution in electrolysis mode. It is interesting to note, in the third plot from the bottom, that around hours 100 to 120, the electrolysis mode reaches a minimum safety voltage, as the cell voltage has dropped below the minimum allowable level, causing the SOE mode to disconnect, and the energy is instead diverted to the grid.

Comparing Figures 5 and 6, it is possible to observe that the rSOCs operation varies significantly depending on whether they are powered by solar or wind energy. Solar energy cycles show extended periods of SOFC operation, whereas wind energy cycles emphasize the electrolysis mode of operation. Although solar energy enables participation in hydrogen markets, its energy contribution only during daylight hours results in lower market participation compared to wind energy.

4.2. Monthly revenue analysis in wind- and solar-dominated microgrids

Given the substantial volume of data generated from a monthly analysis with the considered sampling intervals ranging between 10 and 15 minutes, the second part of the results analysis is conducted using statistical tools. Specifically, the months of May for solar energy and October for wind energy have been selected to facilitate a comparative analysis of the rSOC operation modes corresponding to each type of generation. This allows us to make an assessment of the potential revenue increase associated with each market participation.

The analysis is presented in Figures 8 and 9 for wind and solar energy, respectively. Both figures are divided into three parts: a), b), and c). Subfigures a) shows the percentage of time corresponding to each operation mode of the rSOC, and subfigures b) to the duration of the periods of time in which energy is purchased and sold. It is noted that the rSOC states

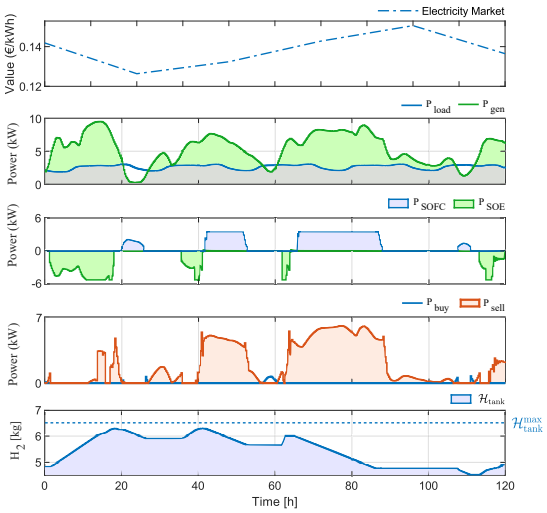

Figure 6: An analysis of the system's operation during windy days considering only the electricity market prices, highlighting a bit higher participation of the SOFC mode (34.49%), and the SOE mode (26.35%).

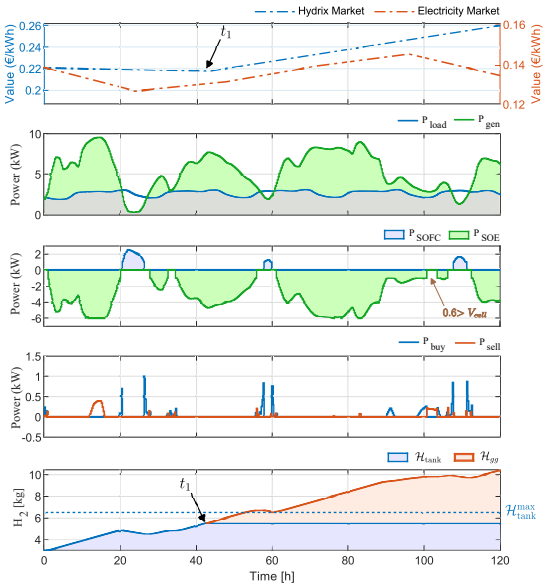

Figure 7: An analysis of the system's operation during windy days considering an electricity and hydrogen market price, highlighting a higher participation of the SOE mode (79.2%), compared to the SOFC mode (9.4%). The signal t_1 indicates an increased revenue trend shift in the hydrogen markets

must sum to 100% of the operation time, as the system is considered to be in the warm zone during operation. For simplicity, non-power-contributing states STB and TCC have been combined into one. Finally, regarding the operating modes in a) and b), as well as the amount of power sold to the grid or used for hydrogen production at each corresponding price, an economic comparison of each mode is presented in section c) in the form of a pie chart, where the percentages are shown relative to the total.

It is noteworthy that in the case of wind energy, Figure 8, participation in the hydrogen market leads to a significant increase in the operating time of the SOE mode. This is because the revenue from selling hydrogen is higher than that from selling electricity. Consequently, the power sold to the grid decreases considerably as the surplus energy is allocated to hydrogen production. Specifically, selling hydrogen in electrolysis mode results in a 14.31% increase in revenue compared to selling electricity. This shift towards electrolysis also leads to a reduction in the fuel cell mode operation.

In the case of solar energy, Figure 9, the differences are less pronounced. This is mainly due to the diurnal pattern of solar generation and the absence of generation at night, which necessitates more frequent use of the fuel cell mode compared to wind energy in both scenarios. While there is an increase in the SOE mode when hydrogen prices are considered, it is only slightly offset by a decrease in the power sold to the grid and does not result in the complete absence of the SOFC mode. Although the overall differences in the solar energy scenario are not very significant, the higher hydrogen market prices still yield a 4.67% increase in final profit compared to considering only the electricity markets. This fact highlights the economic advantage of integrating hydrogen production into renewable energy systems, especially in markets with higher hydrogen prices.

Conclusions

This article has introduced a tertiary predictive control strategy designed for the operation of reversible oxide cells in solar and wind-dominated microgrids based on hydrogen and electricity markets. The model predictive control strategy works with a forecaster and relies on a model validated with experimental data, to determine the most efficient switching between fuel cell and electrolyzer modes. The findings of the analysis are as follows:

- ☑ Solar energy exhibits more predictable mode-switching events and shorter response times of the reversible solid oxide cells compared to wind energy, based on analyzed profiles.
- ☑ In scenarios solely focused on electricity markets, situations dominated by SOFC mode operation arise. Notably, hydrogen production may rely on grid energy during specific operational periods, such as nighttime with solar energy. Numerically, employing generation data from Spain, the algorithm achieves a ≈59% utilization in SOFC mode and ≈23% in SOE mode for solar-based microgrids, with ≈18% of the time allocated to transitions or standby operation. In wind-powered systems, the distribution is slightly different, with ≈51% in SOFC mode, ≈37% in SOE mode, and ≈12% dedicated to transitions or standby.
- ☑ The consideration of both hydrogen and electricity markets alters system operation, favoring the SOE mode over the SOFC mode due to limitations on grid hydrogen absorption. Wind energy demonstrates more significant contributions to hydrogen supply chains compared to

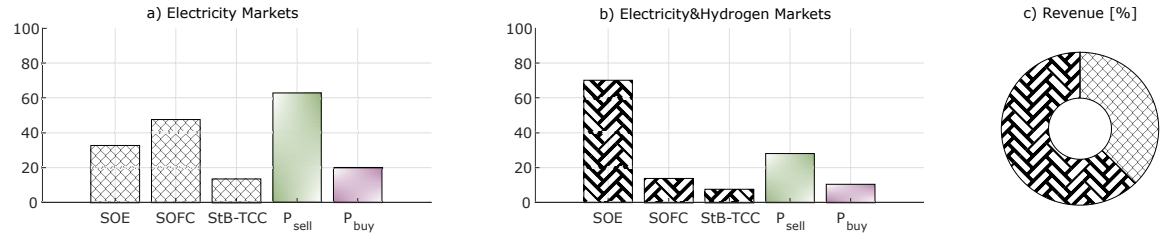

Figure 8: Analysis of the percentage of operation time during a month (October) considering the renewable power comes only from wind energy. The first three bars indicate the percentage of operation time for the three rSOC states, whereas the last two bars indicate the percentage of time in which the energy is bought and sold to the grid. Subfigure a) corresponds to a scenario without participation in hydrogen markets, b) to a scenario with participation in hydrogen markets, and c) revenue comparison

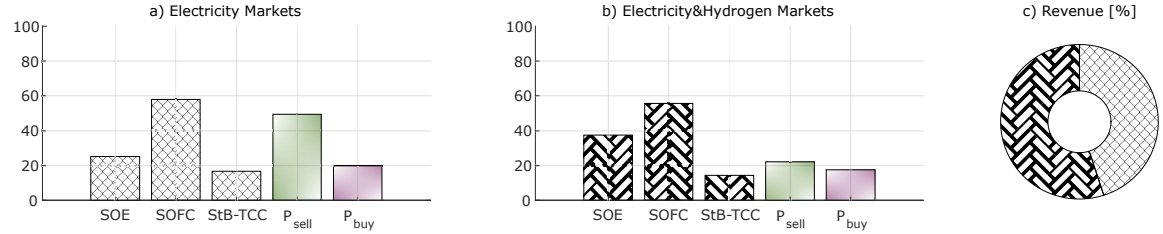

Figure 9: Analysis of the percentage of operation time during a month (May) considering the renewable power comes only from solar energy. The first three bars indicate the percentage of operation time for the three rSOC states, whereas the last two bars indicate the percentage of time in which the energy is bought and sold to the grid. Subfigure a) corresponds to a scenario without participation in hydrogen markets, b) to a scenario with participation in hydrogen markets, and c) revenue comparison

solar energy, attributed to pricing predictability and operational strategies.

- ☑ The performance of the rSOC in electricity or hydrogen markets is viable, depending on the generation capacity factor. In scenarios with a local tank and electricity market orientation, installations dominated by solar or wind energy achieve optimal results. However, when participating in both hydrogen and electricity markets, considering the SOE operating mode based on generation dynamics and market prices proves most beneficial, especially if gas absorption from the pipelines is not assumed. Future research should explore the integration of these systems into gas markets (e.g. methane with some part of hydrogen) to further enhance their operational modes. Despite variations in electricity and hydrogen market prices, it is notorious that the variability of renewable energy sources (mainly wind) results in an increased revenue for the reversible oxide cell.

Acknowledgements

The research leading to these results has received financial support from the European Union's Horizon 2020 research and innovation program under Grant Agreement No. 101101418 (24/7 ZEN), from the Research and Universities Department of Catalonia Government under FI2024 program with grant agreement 2024-FI_3-00930, and from the MCIN/AEI/10.13039/501100011033 and the European Union "NextGenerationEU"/PRTR with gran agreement RYC2021-033477-I.

References

[1] MB Mogensen, M Chen, HL Frandsen, C Graves, JB Hansen, KV Hansen, A Hauch, T Jacobsen, SH Jensen, TL Skafte, et al. Reversible solid-oxide cells for clean and sustainable energy. *Clean Energy*, 3(3):175–201, 2019.

[2] Søren Højgaard Jensen, Christopher Graves, M Mogensen, C Wendel, R Braun, G Hughes, Z Gao, and Scott A Barnett. Large-scale electricity storage utilizing reversible solid oxide cells combined with underground storage of co 2 and ch 4. *Energy & Environmental Science*, 8(8):2471–2479, 2015.

[3] Joshua Mermelstein and Oliver Posdziech. Development and demonstration of a novel reversible sofc system for utility and micro grid energy storage. *Fuel Cells*, 17(4):562–570, 2017.

[4] Konstantin Schwarze, Oliver Posdziech, Simon Kroop, Nieves Lapeña-Rey, and Joshua Mermelstein. Green industrial hydrogen via reversible high-temperature electrolysis. *ECS Transactions*, 78(1):2943, 2017.

[5] Konstantin Schwarze, Oliver Posdziech, Joshua Mermelstein, and Simon Kroop. Operational results of an 150/30 kw rsoc system in an industrial environment. *Fuel Cells*, 19(4):374–380, 2019.

[6] M Califano, M Sorrentino, MA Rosen, and C Pianese. Optimal heat and power management of a reversible solid oxide cell based microgrid for effective technoeconomic hydrogen consumption and storage. *Applied Energy*, 319:119268, 2022.

[7] F Vitale, N Rispoli, M Sorrentino, MA Rosen, and C Pianese. On the use of dynamic programming for optimal energy management of grid-connected reversible solid oxide cell-based renewable microgrids. *Energy*, 225:120304, 2021.

[8] Chunjun Huang, Goran Strbac, Yi Zong, Shi You, Chresten Træholt, Nigel Brandon, Jiawei Wang, and Hossein Ameli. Modeling and optimal operation of reversible solid oxide cells considering heat recovery and mode switching dynamics in microgrids. *Applied Energy*, 357:122477, 2024.

[9] M Califano, M Sorrentino, and C Pianese. Energy management control strategies addressing the rsoc degradation phenomena in a polygeneration microgrid. *International Journal of Hydrogen Energy*, 2024.

[10] M Califano, F Califano, M Sorrentino, MA Rosen, and C Pianese. Hydrogen-based microgrid: Development of medium level controls in a multilevel algorithm framework. *International Journal of Hydrogen Energy*, 52:1173–1189, 2024.

[11] Murphy M Peksen. Exploring the thermomechanical and dynamical mode switch transition of a reversible solid oxide cell. *International Journal of Hydrogen Energy*, 81:353–370, 2024.

[12] Felix Garcia-Torres, Luis Valverde, and Carlos Bordons. Optimal load sharing of hydrogen-based microgrids with hybrid storage using model-predictive control. *IEEE Transactions on Industrial Electronics*, 63(8):4919–4928, 2016.

[13] Pablo Velarde, L Valverde, Jose Maria Maestre, Carlos Ocampo-Martínez, and C Bordons. On the comparison of stochastic model predictive control strategies applied to a hydrogen-based microgrid. *Journal of Power Sources*, 343:161–173, 2017.

[14] Muhammad Bakr Abdelghany, Valerio Mariani, Davide Liuzza, and Luigi Glielmo. Hierarchical model predictive control for islanded and grid-connected microgrids with wind generation and hydrogen energy storage systems. *International Journal of Hydrogen Energy*, 51:595–610, 2024.

[15] Muhammad Bakr Abdelghany, Ahmed Al-Durra, Hatem Zeineldin, and Jiefeng Hu. Integration of cascaded coordinated rolling horizon control for output power smoothing in islanded wind–solar microgrid with multiple hydrogen storage tanks. *Energy*, 291:130442, 2024.

[16] Konrad Motylinski, Jakub Kupecki, Bart Numan, Yashar S Hajimolana, and Vikrant Venkataraman. Dynamic modelling of reversible solid oxide cells for grid stabilization applications. *Energy Conversion and Management*, 228:113674, 2021.

[17] F Tietz, D Sebold, A Brisse, and J Schefold. Degradation phenomena in a solid oxide electrolysis cell after 9000 h of operation. *Journal of Power Sources*, 223:129–135, 2013.

[18] Elisa Zanchi, Antonio Gianfranco Sabato, Mari Carmen Monterde, Lucile Bernadet, Marc Torrell, José Antonio Calero, Albert Tarancón, and Federico Smeacetto. Electrophoretic deposition of MnCo2O4 coating on solid oxide cell interconnects manufactured through powder metallurgy. *Materials & Design*, 227:111768, 2023.

[19] L. Bernadet, G. Gousseau, A. Chatroux, J. Laurencin, F. Mauvy, and M. Reytier. Influence of pressure on solid oxide electrolysis cells investigated by experimental and modeling approach. *International Journal of Hydrogen Energy*, 40(38):12918–12928, 2015.

[20] Jérôme Aicart, Stéphane Di Iorio, Marie Petitjean, Pascal Giroud, Géraldine Palcoux, and Julie Mougin. Transition cycles during operation of a reversible solid oxide electrolyzer/fuel cell (rsoc) system. *Fuel Cells*, 19(4):381–388, 2019.

[21] S Srikanth, MP Heddrich, S Gupta, and KA Friedrich. Transient reversible solid oxide cell reactor operation–experimentally validated modeling and analysis. *Applied Energy*, 232:473–488, 2018.

[22] Ro Peters, M Frank, W Tiedemann, Ingo Hoven, Robert Deja, N Kruse, Q Fang, L Blum, and Ra Peters. Long-term experience with a 5/15kw-class reversible solid oxide cell system. *Journal of the Electrochemical Society*, 168(1):014508, 2021.

[23] Hector del Pozo Gonzalez, Lucile Bernadet, Marc Torrell, Fernando D Bianchi, Albert Tarancón, Oriol Gomis-Bellmunt, and Jose Luis Dominguez-Garcia. Power transition cycles of reversible solid oxide cells and its impacts on microgrids. *Applied Energy*, 352:121887, 2023.

[24] Hector del Pozo Gonzalez, Marc Torrell, Lucile Bernadet, Fernando D Bianchi, Lluís Trilla, Albert Tarancón, and Jose Luis Domínguez-García. Mathematical modeling and thermal control of a 1.5 kw reversible solid oxide stack for 24/7 hydrogen plants. *Mathematics*, 11(2):366, 2023.

[25] FR Bianchi, B Bosio, F Conte, S Massucco, G Mosaico, G Natrella, and M Saviozzi. Modelling and optimal management of renewable energy communities using reversible solid oxide cells. *Applied Energy*, 334:120657, 2023.

[26] Chris Chatfield and Mohammad Yar. Holt-winters forecasting: some practical issues. *Journal of the Royal Statistical Society Series D: The Statistician*, 37(2):129–140, 1988.

[27] European Energy Exchange AG. Eex hydrogen market. https://www.eex-transparency.com/hydrogen. Leipzig, Germany.

[28] Jason Jonkman. The new modularization framework for the fast wind turbine cae tool. In *51st AIAA aerospace sciences meeting including the new horizons forum and aerospace exposition*, page 202, 2013.

[29] Johan Lofberg. Yalmip: A toolbox for modeling and optimization in matlab. In *Proc. of the IEEE international conference on robotics and automation*, pages 284–289, 2004.

[30] LLC Gurobi Optimization. Gurobi optimizer reference manual, 2021.